RSC Advances

ROYAL SOCIETY OF CHEMISTRY

PAPER

View Article Online
View Journal | View Issue

Cite this: *RSC Adv.*, 2024, **14**, 10726

Luminescence properties of a green-emitting mechanoluminescent phosphor $CaSrGa_4O_8$:$x$$Tb^{3+}$ without pre-excitation†

Rui Shi,[ab] Wei Liu,[ac] Lin Li,[ab] Huan Li,[ab] Zhijun Zhang,[ab] Guanghui Rao*[abc] and Jingtai Zhao*[abc]

Received 6th March 2024
Accepted 21st March 2024

DOI: 10.1039/d4ra01745e

rsc.li/rsc-advances

In this study, both mechanoluminescence (ML) and long persistent luminescence (LPL) characteristics were first observed in $CaSrGa_4O_8$ doped with Tb^{3+} ions, which confirmed that $CaSrGa_4O_8$ is a high-quality host for luminescent material research. Notably, the samples show stronger mechanoluminescent intensity with increasing Tb^{3+} doping. Additionally, the introduction of Tb^{3+} led to a shift of the thermoluminescence peak towards higher temperatures and a substantial increase in its intensity, suggesting that Tb^{3+} doping enhances the overall trap concentration and introduces deeper trap energy levels. Presumably, the free carriers in the system recombine upon mechanical stimulation, releasing energy that is transferred to Tb^{3+} ions. Investigations into the intrinsic structure, matrix effects, and trap evolution of the material confirmed that deep and shallow traps are responsible for the observed ML and LPL phenomena, respectively. The elucidation of the unique luminescent properties of the material provides us with some guidance for the development of new multi-functional luminescent materials.

1. Introduction

Mechanoluminescent (ML) materials, which emit light under the mechanical stimulation of external forces, emerge as a significant innovation in this context. Characterized by their linearity, sensitivity, repeatability, and ductility, ML materials efficiently harness mechanical energy, which is abundant in daily life.[1] Mechanoluminescent (ML) materials are stimulation-responsive materials, which can produce different detectable signals in rapid response to various external stimuli (including stretching, compression, bending, *etc.*).[2–5] In recent years, ML materials have shown broad application prospects in the fields of illumination display,[6] information anti-counterfeiting,[7] visual mechanical sensing,[8] structural defects monitoring,[9–11] and genetic detection,[12] and its potential application fields include damage detection,[13] self-diagnosis,[14] defect recording,[15] earthquake prediction,[16] *etc.*, attracting widespread research interest. After securing patents for layered mechanoluminescent materials in doped CaZnOS systems, our continuous research has been carried out to broaden the luminescence range and application potentials of mechanoluminescent materials.[17–19] A novel application involves coating structures with a composite of ML materials and elastic polymers. This technique enables real-time visual observation of surface stress distribution across scales, from nanometers to kilometers. It is particularly beneficial for urban building safety, allowing for visualizing invisible defects and cracks in macro-infrastructure such as high-pressure vessels, pipelines, bridges, and buildings. The emission spectrum of ML phosphors ranges from ultraviolet to near-infrared.[20,21]

Recent advancements spotlight that alkali earth metal gallate compounds, known for their abundant structures, low phonon energy, high flexibility of doping sites in the structures and appropriate bandwidth for adjusting the defect levels with abundant traps, may constitute a large group of host compounds for exploration of ML materials. Their low synthesis temperature and relatively high stability will also be an advantage.[22] Their cost-effectiveness and eco-friendliness have become a central focus of contemporary research efforts.[23–28] Rare earth ions have strong light absorption capacity and high photoelectric conversion efficiency.[29] Given that green is one of the colors most easily captured by the human eye, developing green-emitting ML materials has become a priority.[30,31] Among a variety of rare earth ions or transition metal ions, Tb^{3+} belongs to the typical $^5D_4$–^7F_J ($J = 0, 1, 2, 3, 4, 5, 6$) transition, with their rich emission levels and effective activation in green luminescent materials, are particularly promising.[31] In addition, Tb^{3+} also has a cross-relaxation transition, which provides theoretical support for luminescence with colorful evolution.[32] In

---

[a] School of Materials Science and Engineering, Guilin University of Electronic Technology, Guilin 541004, China. E-mail: rgh@guet.edu.cn; jtzhao@guet.edu.cn

[b] Guangxi Key Laboratory of Information Materials, Guilin University of Electronic Technology, Guilin 541004, China

[c] School of Mechanical and Electrical Engineering, Guilin University of Electronic Technology, Guilin 541004, China

† Electronic supplementary information (ESI) available. See DOI: https://doi.org/10.1039/d4ra01745e

consideration of the above discussions, $CaSrGa_4O_8$ (CSGO) has been used as a mechanoluminescent host in our research, and it has already shown good perspectives in other doping systems.[33–35]

In this work, a series of green emission phosphors $Ca_{1-x}SrGa_4O_8{:}xTb^{3+}$ (CSGOT) have been successfully synthesized. With the concentration of Tb^{3+} doped, these phosphors exhibit a rich energy level spectrum in the range of 450–650 nm, indicating diverse energy level transitions. This new class of mechanoluminescent materials, which requires no pre-excitation, shows great potential for application.

2. Experimental section

2.1. Materials and synthesis

Polycrystalline powders with the formula of $Ca_{1-x}SrGa_4O_8{:}xTb^{3+}$ (x = 0, 0.03, 0.05, 0.07, 0.09 and 0.11) were synthesized by convention a high-temperature solid-state reaction. The starting materials Ca_2CO_3 (Aladdin, 99.99%), Sr_2O_3 (Aladdin, 99.95%), Ga_2O_3 (Aladdin, 99.99%), Tb_4O_7 (Aladdin, 99.99%) were weighted out according to the stoichiometric ratio. These powders were then mixed and ground in an agate mortar using anhydrous ethanol for about 30 min. After mixing, the powders were placed in a crucible and dried in an oven for 15 min to evaporate any remaining anhydrous ethanol. The dried mixtures were then transferred to a corundum crucible and sintered at 1280 °C for 10 hours, with a heating rate of 5 °C min^{-1} under air. Once the furnace cooled naturally to room temperature, the products were removed and ground into fine powders for subsequent measurements.

Then, 1.5 g of Polydimethylsiloxane (PDMS) precursor, 0.15 g of curing agent, and 1.0 g of synthesized phosphor were weighed and combined to create the composite elastomer. The mixture was stirred mechanically for 10 min. Subsequently, it was cured in an oven at 80 °C for 2 hours, resulting in the $Ca_{1-x}SrGa_4O_8{:}xTb^{3+}$/PDMS composite elastomer, ready for ML examining.

2.2. Characterization

The phase purity of each sample was checked by X-ray diffraction patterns (XRD) collected on a powder X-ray diffractometer (Cu K_α, λ = 1.54178 Å) with a scanning step size of 0.02626°, range of 10–90°. The morphology and elemental distribution of the powder samples were analyzed by scanning electron microscopy (SEM, FEG-450) equipped with energy dispersive X-ray spectroscopy (EDS). The diffuse reflectance (DR) spectra were measured by using a UV-VIS-NIR spectrophotometer (U-3900H Hitachi) and calibrated with $BaSO_4$ as the standard reference. Photoluminescence excitation (PLE), photoluminescence (PL) and the time-gated photoluminescence decay curve were recorded *via* a fluorescence spectrometer (FLS1000 Edinburgh) equipped with a 450 W Xe lamp as the steady-state excitation source. The weight of the measured samples was constant (200 mg). The long afterglow decay curves and thermoluminescence (TL) curves were recorded using a fluorescence spectrometer and thermo-luminescence meter (TOSL-3DS). Before the TL measure, the samples were first exposed to the radiation from the UV light for 5 min and then heated from room temperature to 200 °C at a rate of 2 °C s^{-1}. X-ray photoelectron spectroscopy (XPS) (ESCALAB 250xi, ThermoFisher) was used to analyze the chemical bonding states. The mechanoluminescence (ML) spectra were recorded by a motion controller, a photocounting system (QE-Pro Ocean Optics) and a computer.

3. Results and discussion

3.1. Phase, structure and morphology

The XRD patterns of $Ca_{1-x}SrGa_4O_8{:}xTb^{3+}$ (x = 0, 0.03, 0.05, 0.07, 0.09 and 0.11) samples are shown in Fig. 1(a). According to the Hume-Rothery rules, a solid solution is viable if the atomic radius difference between the solute and solvent ions is within 30%. The ionic radius difference is calculated using the formula (1):[36,37]

$$D_r = 100\% \times \left[\frac{R_m(C_N) - R_d(C_N)}{R_m(C_N)}\right] \tag{1}$$

where D_r is the percentage difference of radius, R_m (C_N) is the radius of the main ion to be replaced, and R_d (C_N) is the radius of the doped ion. Considering the valence and ionic radius of Tb^{3+} ions (for $C_N = 6$, r = 0.92 Å) and Ca^{2+} ions (for $C_N = 6$, r = 1.00 Å), and the larger difference with Sr^{2+} ions (for $C_N = 6$, r = 1.18 Å), Tb^{3+} ions are more likely to replace the Ca^{2+} ions in the lattice. The calculated values of D_r (Ca^{2+}–Tb^{3+}) = 8%, and D_r (Sr^{2+}–Tb^{3+}) = 22.03%, respectively, indicating a preferential replacement of Ca^{2+} by Tb^{3+} in the $Ca_{1-x}SrGa_4O_8{:}xTb^{3+}$ structure. Without the sufficient crystal size for single crystal X-ray diffraction, experimental data was consistent with the structural data obtained by Wang's group confirming that the doping with Tb^{3+} ions did not introduce any impurity phase in Fig. 1(a). By indexing the XRD data for $Ca_{0.93}SrGa_4O_8{:}0.07Tb^{3+}$, it is obtained that a = 15.841(6) Å, b = 8.311(4) Å, c = 9.028(5) Å, β = 90.60(3)°, V = 1188.6(6) $Å^3$. Refined cell lattice parameters ($a/b/c/\beta/V$) with different concentrations of Tb^{3+} ions doping shown in Fig. S1(a–e).† The experimental and computational XRD patterns of crystal structure model of $Ca_{0.93}SrGa_4O_8{:}0.07Tb^{3+}$ shown in Fig. 1(b), indicating the purities of the phases and the correctness of the crystal structure model proposed in monoclinic system with space group $P2_1$.[34]

The surface morphology, grain size and crystallinity of phosphors play an important role in the luminescence properties of phosphors. The microscopic morphology of $Ca_{1-x}SrGa_4O_8{:}xTb^{3+}$ was characterized by SEM at 1.2k× and 20k× magnification in Fig. 1(c and e). The phosphor particles shown in Fig. 1(e) have irregular polyhedral morphology and range in size from several microns. The SEM image of captured $Ca_{0.93}SrGa_4O_8{:}0.7Tb^{3+}$ shows no agglomeration and no impurities. This is suitable for producing excellent ML phenomena. The EDS Spectroscopy conducted on the selected area in Fig. 1(d and e) demonstrated the uniform distribution of Ca, Sr, Ga, O, and Tb within the analyzed region. This observation provides convincing evidence that the desired sample was successfully synthesized, confirming that the dopant ions were effectively

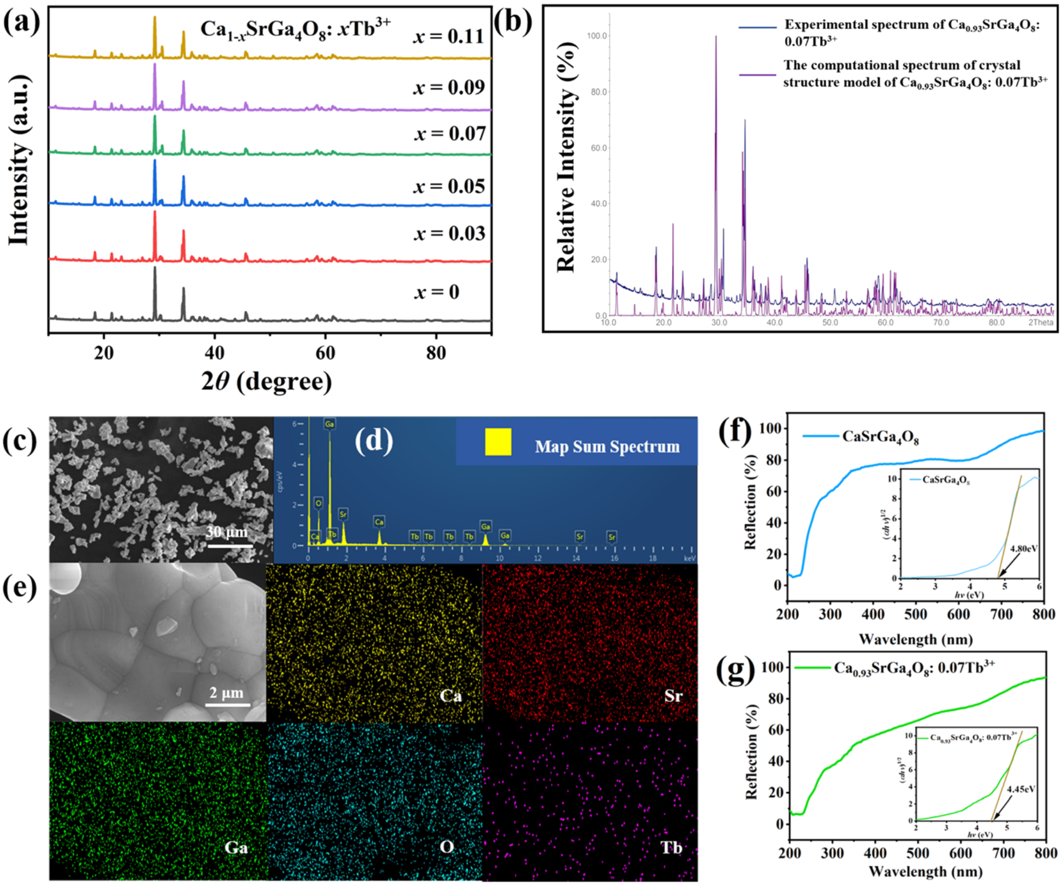

Fig. 1 (a) XRD patterns of the $Ca_{1-x}SrGa_4O_8{:}xTb^{3+}$. (b) Comparison of experimental XRD pattern of $Ca_{0.93}SrGa_4O_8{:}0.07Tb^{3+}$ sintered at 1280 °C with the calculated pattern. (c) SEM micrograph of $Ca_{0.93}SrGa_4O_8{:}0.07Tb^{3+}$ (scale bar: 30 μm; magnification: 1.2k×). (d) EDS energy spectrum of $Ca_{0.93}SrGa_4O_8{:}0.07Tb^{3+}$. (e) SEM micrograph of $Ca_{0.93}SrGa_4O_8{:}0.07Tb^{3+}$ (scale bar: 2 μm; magnification: 20k×), the SEM mapping images of elements O, Sr, Ca, Ga and Tb, respectively. (f) Diffuse reflectance spectra of $CaSrGa_4O_8$. (g) Diffuse reflectance spectra of $Ca_{0.93}SrGa_4O_8{:}0.07Tb^{3+}$.

incorporated into the CSGO crystal structure. The uniform distribution of elements further confirms the formation of well-integrated and chemically homogeneous materials, thereby enhancing the reliability and quality of the synthesis process.

Fig. 1(f) displays the diffuse reflectance spectra of $CaSrGa_4O_8$ across a wavelength range from 200 nm to 800 nm. When compared to the diffuse reflectance spectra of $Ca_{0.93}SrGa_4O_8{:}0.07Tb^{3+}$ shown in Fig. 1(g), it can be deduced that the absorption band for $Ca_{0.93}SrGa_4O_8{:}0.07Tb^{3+}$ in the 240–260 nm range is due to host absorption, while the absorption band in the 290–350 nm range is attributed to the transition absorption of Tb^{3+} by Fig. S2.†

This diagram is used to calculate the band gap (E_g) of both $CaSrGa_4O_8$ and $Ca_{0.93}SrGa_4O_8{:}0.07Tb^{3+}$. The E_g can be calculated based on the following eqn (2):[35]

$$(\alpha h\nu)^2 = A(h\nu - E_g) \tag{2}$$

In this equation, $h\nu$ represents the energy of the incident photon, α is the Kubelka–Munk function corresponding to absorbance, and A is a constant. The Kubelka–Munk function can be determined by the following formula (3):[35]

$$\alpha = \frac{(1-R)^2}{2R} \tag{3}$$

R denotes the reflectance. Based on these calculations, the optical bandgap of the host material $CaSrGa_4O_8$ is estimated to be 4.80 eV, while that of the doped $Ca_{0.93}SrGa_4O_8{:}0.07Tb^{3+}$ is reduced to 4.45 eV.

The narrowing of the optical bandgap in the doped material is significant. It suggests that electrons are more easily excited from the valence band to the conduction band under ultraviolet (UV) excitation, potentially leading to enhanced photoluminescence (PL) emission.[36] Additionally, the impurity energy levels introduced by the doped Tb^{3+} ions may attributed to enhanced energy transfer between the $[GaO_4]$ group and Tb^{3+} ions, leading to more excited electrons returning to the ground state to this bandgap narrowing. This alteration in the bandgap could significantly impact the ML properties and the intensity of ML emissions. These changes underscore the influence of doping on the electronic structure and optical properties of these materials, with potential implications for their practical applications in fields.

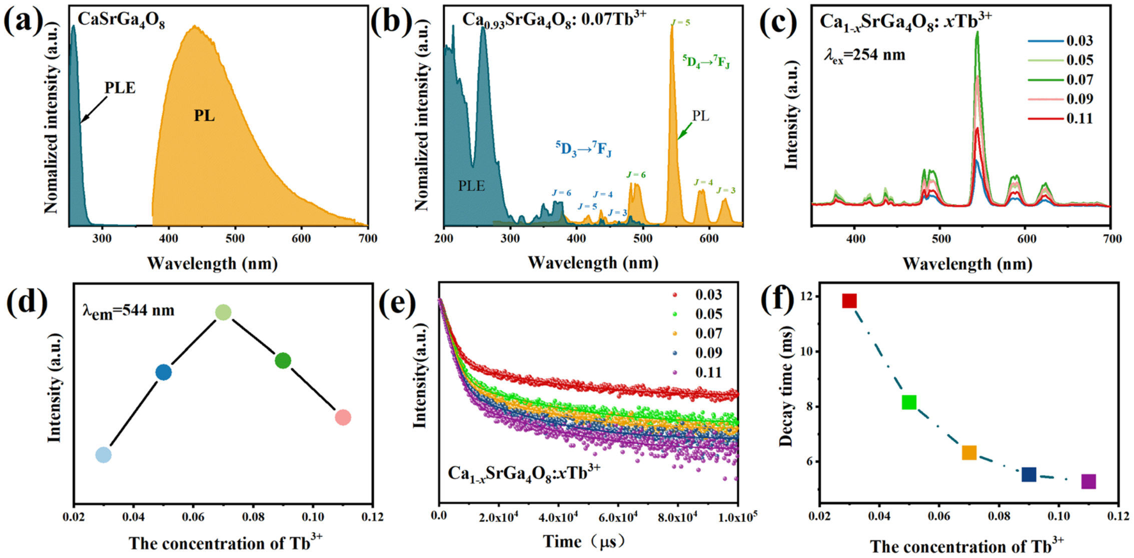

Fig. 2 (a) PLE and PL spectra of the CaSrGa$_4$O$_8$ at room temperature. (b) PLE and PL spectra of the Ca$_{0.93}$SrGa$_4$O$_8$:0.07Tb^{3+} at room temperature. (c) The PL spectra of Ca$_{1-x}$SrGa$_4$O$_8$:xTb^{3+}. (d) Dependence of emission peak (544 nm) intensities *versus* Tb^{3+} ion content. (e) PL decay curves under 254 nm excitation of the Ca$_{1-x}$SrGa$_4$O$_8$:xTb^{3+}. (f) PL decay curves of Ca$_{1-x}$SrGa$_4$O$_8$:xTb^{3+} ($\lambda_{ex} = 254$ nm, $\lambda_{em} = 544$ nm).

3.2. PL/LPL properties of Ca$_{1-x}$SrGa$_4$O$_8$:xTb^{3+}

In Ca$_{1-x}$SrGa$_4$O$_8$:xTb^{3+}, the excitation and emission spectra of Tb^{3+} ions are depicted in Fig. 2(b), while the undoped sample is presented in Fig. 2(a). Excitation spectra of Ca$_{1-x}$SrGa$_4$O$_8$:xTb^{3+} (x = 0.03, 0.05, 0.07, 0.09 and 0.11) monitored at 544 nm as shown in Fig. S2.† When excited at 254 nm in Fig. 2(b), the phosphors display a series of sharp emission lines that are characteristic of the internal 4f transitions of Tb^{3+} ions, specifically from the ^{5}D$_3$ and ^{5}D$_4$ levels to the ^{7}F$_J$ levels (where J = 3, 4, 5, and 6). The broad excitation spectra, observed by monitoring the emission peaks of the ^{5}D$_4$–^{7}F$_5$ transition at 544 nm, show an asymmetric shape with an acromion and a maximum at approximately 280 nm and 254 nm, respectively. The energy level of the acromion at 280 nm aligns well with the energy absorbed by the main lattice, suggesting an effective energy transfer from the [GaO$_4$] group to the Tb^{3+} ion.[38] The broad peak at 254 nm is primarily due to the combined effects of bulk absorption of Tb^{3+} and the 4f–5d inter-configuration transition of Tb^{3+}, which is spin-allowed. The excitation lines within the 300–400 nm range represent optical transitions within the 4f electron configuration of the Tb^{3+} ion, and their weak intensity is likely due to the correspondingly low vibrational intensity. Notably, the 254 nm excitation peak is significantly stronger than the right acromion. This observation underscores the strong absorption and efficient energy utilization at this wavelength, which is critical for the photoluminescent properties of these materials. This characteristic makes the Ca$_{1-x}$SrGa$_4$O$_8$:xTb^{3+} phosphors particularly suitable for applications requiring efficient excitation and bright luminescence, such as in lighting and display technologies.

The emission spectra of Ca$_{1-x}$SrGa$_4$O$_8$:xTb^{3+} phosphors, as shown in Fig. 2(c), reveal that the luminescence intensity is significantly influenced by the concentration of Tb^{3+} doping. Concentration quenching of Tb^{3+} is observed, indicating that there is an optimal doping concentration for achieving maximum luminescence intensity. This optimal concentration is found to be 0.07 for Tb^{3+}. To differentiate the forbidden transitions from the ^{5}D$_4$ to ^{7}F$_J$ (J = 3, 4, 5, and 6) levels in Tb^{3+} ions, the emission decay curve at 544 nm under 254 nm excitation of CSGOT was measured, with the results presented in Fig. 2(d). These decay curves fit well with second-order exponential functions, described by equation:

$$I(t) = I_0 + A_1\exp\left(\frac{-t}{\tau_1}\right) + A_2\exp\left(\frac{-t}{\tau_2}\right) \tag{4}$$

where I is the emission intensity, A_1 and A_2 are the fitting constants, and τ_1 and τ_2 are the fast and slow decay lifetimes, respectively. The mean luminous lifetime can be evaluated using the following formula.

$$\tau^* = \frac{A_1{\tau_1}^2 + A_2{\tau_2}^2}{A_1\tau_1 + A_2\tau_2} \tag{5}$$

The PL attenuation measurements indicate that CSGOT follows a double exponential decay behavior. The average lifetime of CSGOT, as shown in Fig. 2(e), gradually decreases with varying doping ion concentrations, suggesting complex radiative and non-radiative decay dynamics of the two excited states. Despite these changes, the average lifetime remains at the millisecond level. As the Tb^{3+} ion concentration increases, the τ^* value decreases from 11.83 ms to 5.27 ms in Fig. 2(f), which is attributed to enhanced energy transfer between the [GaO$_4$] group and Tb^{3+} ions, leading to more excited electrons returning to the ground state and it is also a simple concentration quenching effect.[30]

The LPL spectra exhibit similar trends and peak shapes, confirming their origin from the same luminescent Tb^{3+} center

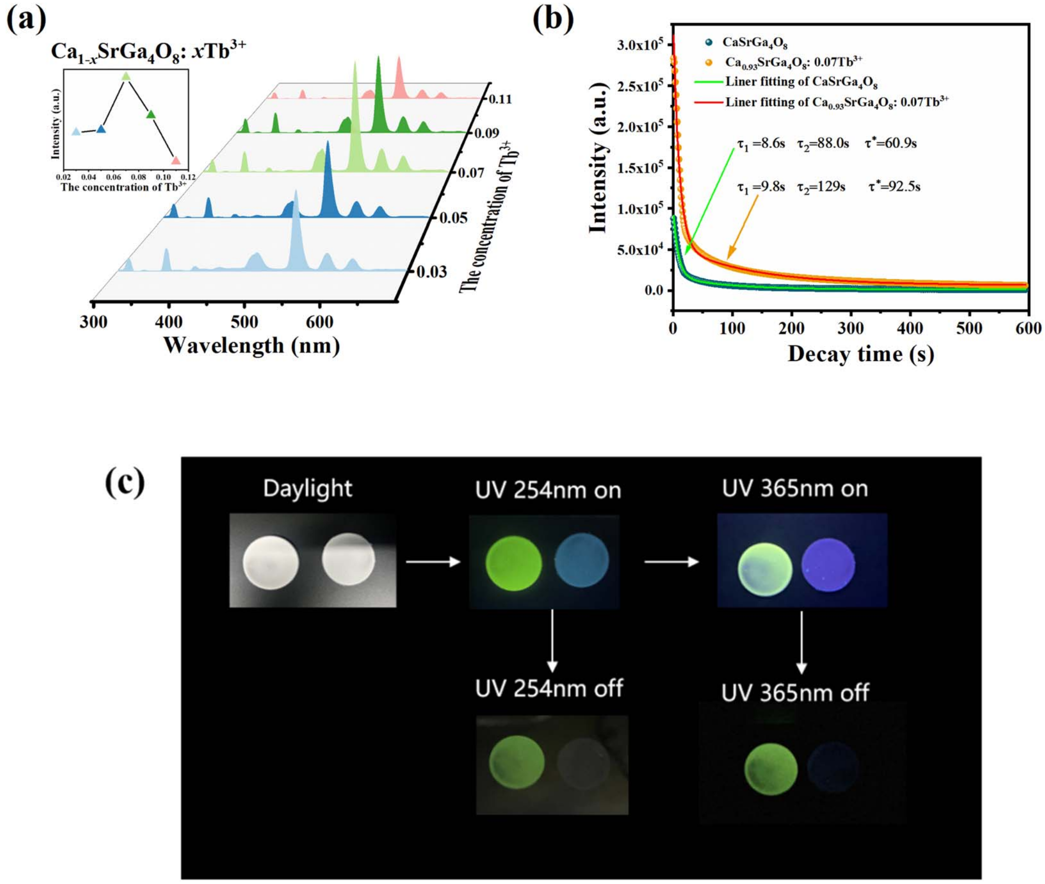

Fig. 3 (a) LPL spectra of the $Ca_{1-x}SrGa_4O_8$:$x$$Tb^{3+}$ and the insets show the LPL emission intensity of the $Ca_{1-x}SrGa_4O_8$:$x$$Tb^{3+}$ ($\lambda_{ex} = 254$ nm, $\lambda_{em} = 544$ nm). (b) LPL lifetime curves of $CaSrGa_4O_8$ and $Ca_{0.93}SrGa_4O_8$:0.07Tb^{3+}. (c) Photographs of the $CaSrGa_4O_8$ and $Ca_{0.93}SrGa_4O_8$:0.07Tb^{3+} under daylight, 254 nm UV light excitation and after the removal of the UV light excitation, 365 nm UV light excitation and after the removal of the UV light excitation.

in Fig. 3(a). The LPL emission spectra of the samples, depicted in Fig. 3(b), display excellent persistent afterglow performance. The behavior suggests the presence of multiple traps in the $Ca_{1-x}SrGa_4O_8$:$x$$Tb^{3+}$ phosphors. The LPL intensity decreases with increasing Tb^{3+} ion doping constantly above $x = 0.07$, due to the nature and concentration of defects.

Under ultraviolet excitation, the undoped phosphor emits blue light, while the doped Tb^{3+} samples exhibit bright green light emission. Notably, an excellent green afterglow is observed after the cessation of UV excitation, highlighting the material's potential for applications requiring persistent luminescence in Fig. 3(b). Under ultraviolet excitation, the $Ca_{1-x}SrGa_4O_8$:$x$$Tb^{3+}$ phosphors absorb energy, leading to the excitation of free electrons from the valence band to the conduction band. Once in the conduction band, these electrons move freely before being captured by traps within the crystal lattice. The electrons trapped in shallow traps begin to be released back into the conduction band upon cessation of the ultraviolet excitation. This release is facilitated by thermal perturbations. These freed electrons then undergo non-radiative recombination with holes (the absence of electrons in the valence band). During this recombination process, the energy is transferred to the Tb^{3+} ions. The transfer of energy to Tb^{3+} ions result in the strong afterglow phenomenon, as depicted in Fig. 3(c). This afterglow is a result of the phosphorescence process, where the delayed recombination of electrons and holes leads to prolonged emission of light after the initial excitation source (in this case, UV light) has been removed.

3.3. ML properties of $Ca_{1-x}SrGa_4O_8$:$x$$Tb^{3+}$

PDMS is commonly utilized as a base material in the fabrication of ML films. Its popularity in this application stems from two key attributes: high transparency and an effective stress transfer capability. These properties make PDMS an ideal medium for observing and studying ML phenomena.[39,40] The ML intensity data and images are shown in Fig. 4 and 5, respectively.

To accurately assess the ML properties of the phosphor and differentiate them from LPL behavior, the phosphors and PDMS were combined to make an elastic film for the ML test in Fig. 5(a), and the ML spectra of the phosphor were measured without any prior UV pre-irradiation. This approach ensures that the observed ML effects are purely due to mechanical stimulation rather than residual effects of earlier light exposure. The ML spectra exhibited a series of green emission peaks corresponding to the electron transitions of $^5D_4$ to ^7F_J ($J = 3$, 4, 5, and 6) in Tb^{3+} ions. The experimental results revealed that the

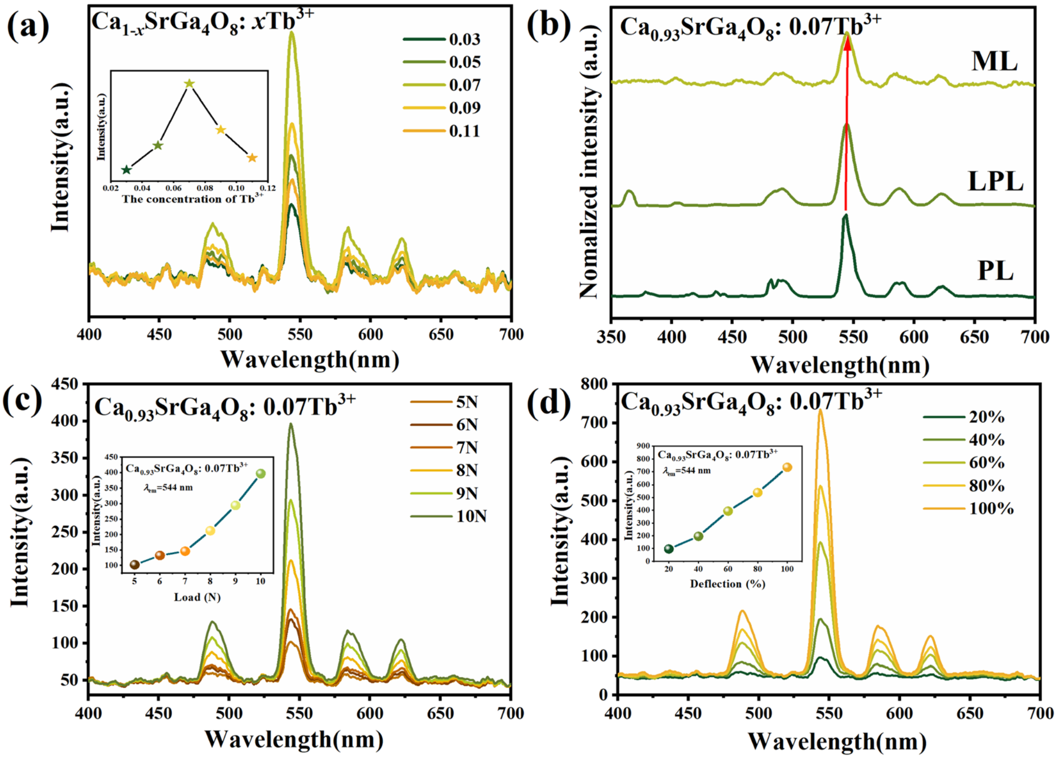

Fig. 4 (a) ML spectra of the $Ca_{1-x}SrGa_4O_8$:$x$$Tb^{3+}$ (the ML emission peak of the $Ca_{1-x}SrGa_4O_8$:$x$$Tb^{3+}$, $\lambda_{em} = 546$ nm, $F = 6$ N, acrylic pen as a direct-acting medium, an approximate friction rate of 3 mm per second). (b) ML, LPL, and PL spectra of the $Ca_{0.93}SrGa_4O_8$:$0.07Tb^{3+}$. (c) ML spectra of the $Ca_{0.93}SrGa_4O_8$:$0.07Tb^{3+}$ with different load. (d) ML spectra of the $Ca_{0.93}SrGa_4O_8$:$0.07Tb^{3+}$ different deflection.

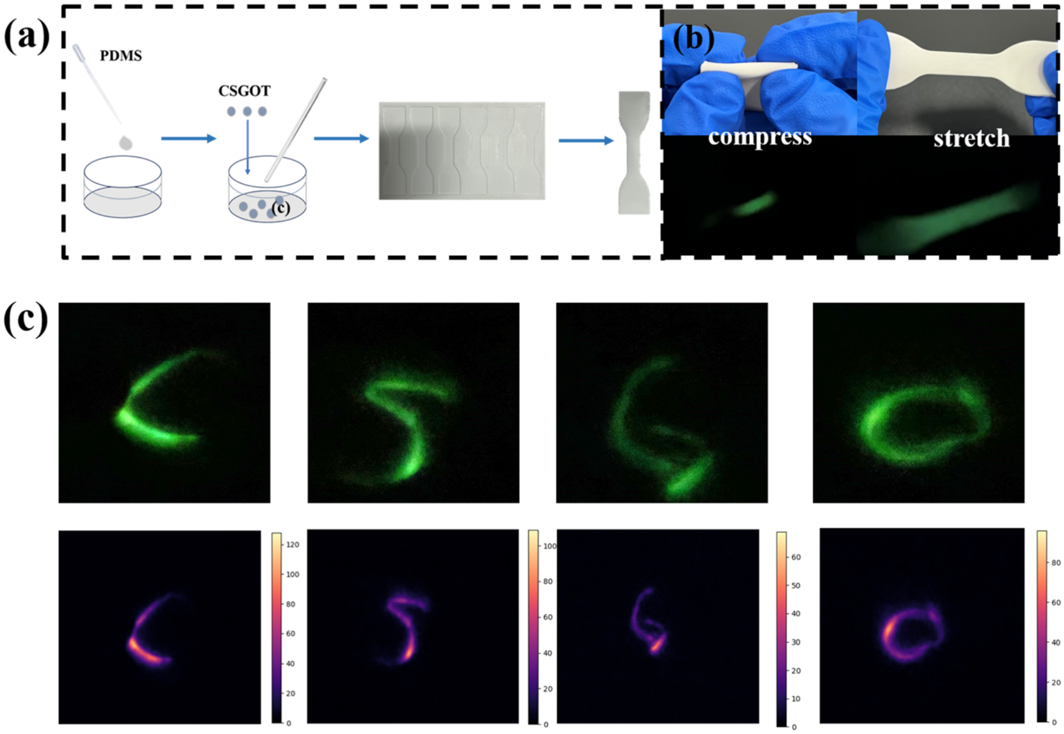

Fig. 5 (a) Preparation process of mechanoluminescent film. (b) The ML photos of $Ca_{0.93}SrGa_4O_8$:$0.07Tb^{3+}$ (compress and stretch). (c) The multi-mode anti-counterfeiting model: using a glass sleeve to write C, S, G, O, respectively.

ML intensity varied with the concentration of Tb^{3+} ions, first increasing and then decreasing, peaking at a concentration of $x = 0.07$ in Fig. 4(a). This trend aligns with the observed patterns in both the LPL and PL spectra, as shown in Fig. 4(b). In Fig. 4(c) and (d), a notable correlation between ML intensity and applied force is observed in the studied film. Specifically, the ML intensity exhibits a progressive increase in response to escalating applied forces. This trend continues until the film reaches a critical force threshold, beyond which it fails. Notably, within a certain force range, the luminous intensity demonstrates a linear relationship with the applied force, indicating a direct and proportional increase in light emission with escalating mechanical stress. This trend is consistently replicated in both figures, underscoring the reproducibility of mechanoluminescent response under varying mechanical stimuli.

An interesting observation regarding the ML spectrum is its slight redshift compared to the PL spectrum, shown in Fig. 4(b). By applying mechanical stimuli on the particles of CSGOT, lattice shrinks and crystal field strengthens. Consequently, crystal field splitting of 5d energy level of Tb^{3+} ions increases and the 5d lowest energy level decreases, resulting in the spectral redshift of Tb^{3+}.[36] This redshift in the ML spectrum under mechanical stress highlights the sensitivity of Tb^{3+} doped $CaSrGa_4O_8$ phosphors to changes in their physical environment, underlining their potential in applications requiring responsive luminescent materials. When stretching or compression force is applied to the flexible film, the bright ML phenomenon is displayed in Fig. 5(b). Characters such as Ca, Sr, Ga, and O are written on the ML film, and the note mapping is also clearly visible. The gray value can be obtained by analyzing

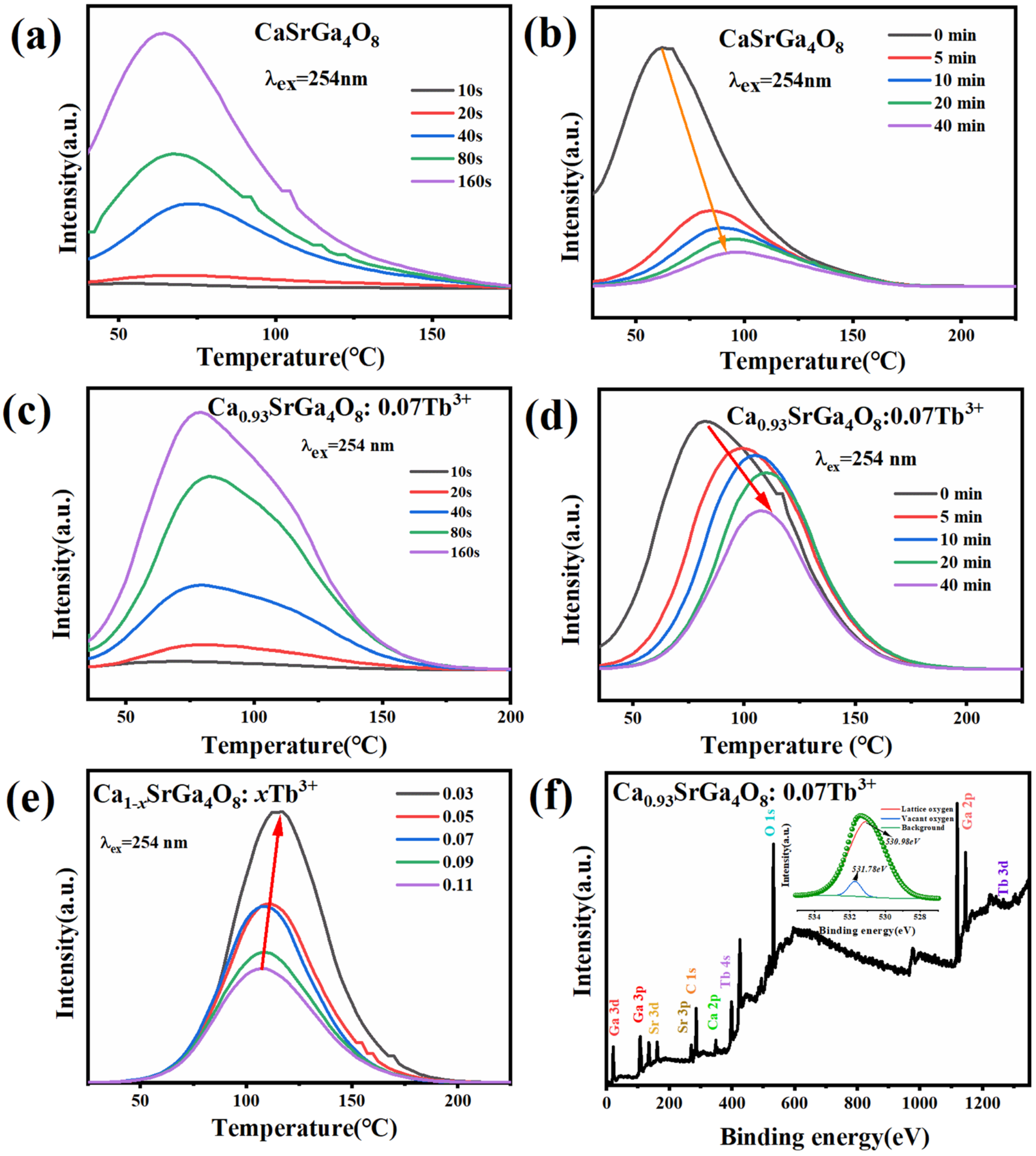

Fig. 6 (a and b) TL curves of $CaSrGa_4O_8$. (c and d) TL curves of $Ca_{0.93}SrGa_4O_8$:$0.07Tb^{3+}$. (e) TL curves of the $Ca_{1-x}SrGa_4O_8$:xTb^{3+} (f) XPS survey spectrum of $Ca_{0.93}SrGa_4O_8$:$0.07Tb^{3+}$ and the insets show the XPS analysis of the O 1s orbital for the $Ca_{0.93}SrGa_4O_8$:$0.07Tb^{3+}$.

the picture, and then the force of the sample can be more intuitively understood in Fig. 5(c).

3.4. TL/XPS properties of $Ca_{1-x}SrGa_4O_8$:$x$$Tb^{3+}$

The luminescence emission spectrum of the $Ca_{1-x}SrGa_4O_8$:$x$$Tb^{3+}$ phosphors demonstrate characteristic line emissions of Tb^{3+} in the 50–200 °C temperature range. This observation confirms that the stored energy is released from heat-activated traps and then recombines with ionized Tb^{3+} ions. With an increase in Tb^{3+} content, there is a notable decrease in the level of shallow traps. This reduction facilitates the easier release of charge carriers under mechanical stimulation, leading to enhanced mechanoluminescent behavior.[36] The average lifetime of CSGOT, as shown in Fig. 2(e), gradually decreases with varying doping ion concentrations in a deeper understanding of the capture and release of electrons in the sample, thermoluminescence spectroscopy tests were conducted, focusing on excitation and decay time. The results, depicted in Fig. 6(a) and (c), show that initially when the traps are almost empty, there is a weak thermoluminescence intensity and emission of green light. However, as the irradiation time increases, both the green emission and thermoluminescence intensity of the sample also increase. This trend suggests that with prolonged excitation, more electrons are trapped, leading to a rise in the thermoluminescence peak. The consistent peak position across different tests indicates that electrons are captured at a similar rate in various traps. After several minutes of excitation, the peak intensity of thermoluminescence stabilizes across all samples, signifying that the traps have reached their electron capacity. Furthermore, as the decay time increases, the thermoluminescence peak shifts towards higher temperatures. Fig. 6(b) and (d) reveal that electron release is faster in shallow traps. In CSGOT, despite higher TL peak intensity, the shallower traps allow trapped electrons to escape more easily to the conduction band (CB), resulting in LPL emission and faster decay.

As the Tb^{3+} doping concentration increases, the depth of the shallow trap's defect level significantly decreases in Fig. 6(e), implying that trapped carriers are more readily released by thermal vibration or mechanical force. This change is attributable to both intrinsic defect $(V''_{Ca}, V^{\bullet\bullet}_{O})$ and extrinsic defects $(Tb^{(3+)\bullet}_{Ca^{2+}})$. The introduction of Tb^{3+} ions also lead to a shift in the thermoluminescence peak towards higher temperatures, along with a significant increase in its intensity. This shift and intensity increase indicate that Tb^{3+} doping not only enhances the overall concentration of traps within the material but also introduces additional deep trap energy levels. These deep trap levels are likely responsible for the observed changes in the thermoluminescence characteristics, reflecting a more complex energy landscape for carrier dynamics within the material. The presence of these deeper traps and the shift in thermoluminescence behavior underscores the significant impact of Tb^{3+} doping on the material's electronic structure and its potential applications in devices that rely on carrier trapping and release mechanisms.

X-ray photoelectron spectroscopy (XPS) is a valuable analytical tool for analyzing the valence states of elements in a sample and recording changes in oxygen vacancy numbers and the surrounding coordination environment. After testing, the data were calibrated to a C 1s electron peak at 284.8 eV. XPS spectroscopy performed at binding energies of 0–1350 eV on the synthesized $Ca_{0.93}SrGa_4O_8$:$0.07Tb^{3+}$ phosphor revealed clear signals of Ca, Sr, Ga, O, and Tb elements in Fig. 6(f). The O 1s orbit could be decomposed into two peaks at 530.98 eV (O_I) and 531.78 eV (O_{II}). The lower binding energy component (O_I) is primarily due to bridge oxygen (lattice oxygen), while the O_{II} peak, which is about 0.8 eV higher in binding energy than O_I, is related to oxygen vacancies. This finding indicates an increase in oxygen vacancies, corroborating the thermoluminescence data that associate shallow traps with oxygen vacancies in the samples.

3.5. ML application demonstration and mechanism investigation

Under ultraviolet excitation, the CIE coordinates of the samples with different doping concentrations remained basically

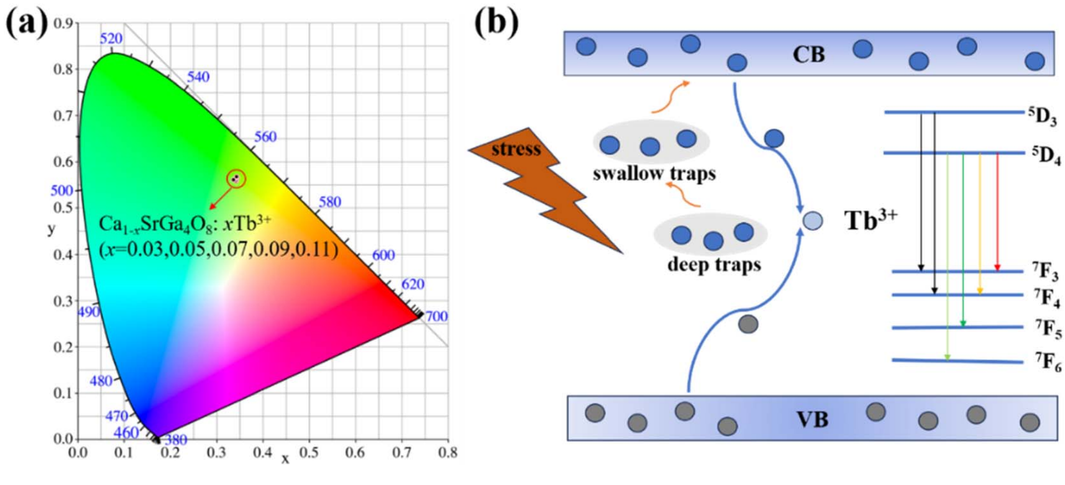

Fig. 7 (a) CIE chromaticity diagram corresponding to the $Ca_{1-x}SrGa_4O_8$:$x$$Tb^{3+}$ emission intensity. (b) ML processes of the $Ca_{1-x}SrGa_4O_8$:$x$$Tb^{3+}$ in the energy level diagram.

unchanged, showing significant green emission in Fig. 7(a). Without mechanical stress, free electrons and holes in the $Ca_{1-x}SrGa_4O_8$:$x$$Tb^{3+}$ phosphors move randomly within their respective conduction and valence bands. However, under mechanical force stimulation, these free electrons and holes combine in proximity to each other, releasing energy in the process. This released energy is then transferred to the Tb^{3+} ions, leading to the occurrence of the ML phenomenon, as depicted in Fig. 7(b). By studying the intrinsic structure, matrix effects, and trap evolution, it is confirmed that deep trap and shallow trap are the causes of the observed ML and LPL, respectively.

4. Conclusion

In summary, $Ca_{1-x}SrGa_4O_8$:$x$$Tb^{3+}$ phosphors have been synthesized and their optical luminescent properties have been investigated. The addition of Tb^{3+} introduces a wealth of trap energy levels and brings excellent long afterglow and stress luminescence properties. Moreover, deep and shallow traps are identified as the primary causes of the observed ML and LPL phenomena, respectively, highlighting the critical role of trap-controlled luminescence processes in optical properties, which brings more possibilities for the materials in note mapping and stress sensing.

Author contributions

Rui Shi: conceptualization, visualization, formal analysis, writing – original draft, project administration. Wei Liu: supervision, data curation, formal analysis, visualization, investigation, writing – review and editing, project administration. Lin Li and Huan Li: data curation, formal analysis, investigation. Zhijun Zhang: supervision, writing – review and editing, project administration. Guanghui Rao and Jingtai Zhao: funding acquisition, project administration, supervision, writing – review and editing.

Conflicts of interest

The authors declare no conflict of interest.

Acknowledgements

This work is supported by the fund from Guangxi Science and Technology Base and Talent Special Project (2020AC18005), Innovation Project of Guangxi Graduate Education (YCSW2022267), Central Government Guided Local Science and Technology Development Fund Project (ZY22096009) and Foundation for Guangxi Bagui scholars.

References

1 Z. Wang, S. Zhao, Y. X. Wang, F. Wang, A. A. Ansari and R. Lv, *Anal. Bioanal. Chem.*, 2023, **1–10**, DOI: **10.1007/s00216-023-04968-1**.
2 B. Chen, X. Zhang and F. Wang, *Acc. Mater. Res.*, 2021, **2**, 364–373.
3 J. C. G. Bünzli and K. L. Wong, *J. Rare Earths*, 2018, **36**, 1–41.
4 Y. Xie and Z. Li, *Mater. Chem. Front.*, 2020, **4**, 317–331.
5 S. M. Jeong, S. Song, H. Kim, K. Joo and H. Takezoe, *Adv. Funct. Mater.*, 2016, **26**, 4848–4858.
6 S. M. Jeong, S. Song, K. I. Joo, J. Kim, S. H. Hwang, J. Jeong and H. Kim, *Energy Environ. Sci.*, 2014, **7**, 3338–3346.
7 M. Y. Wang, H. Wu, W. B. Dong, J. Y. Lian, W. X. Wang, J. Y. Zhou and J. C. Zhang, *Inorg. Chem.*, 2022, **61**, 2911–2919.
8 Z. X. Zhou, K. H. Liu, Z. Y. Ban and W. Z. Yuan, *Composites, Part A*, 2022, **154**, 106806.
9 N. Terasaki and C. N. Xu, *Jpn. J. Appl. Phys.*, 2009, **48**, 04C150.
10 S. Krishnan, H. Van der Walt, V. Venkatesh and V. B. Sundaresan, *J. Intell. Mater. Syst. Struct.*, 2017, **28**, 2458–2464.
11 N. Terasaki, Y. Fujio, Y. Sakata, S. Horiuchi and H. Akiyamaet, *J. Adhes.*, 2018, **94**, 867–879.
12 H. Song, S. Timilsina, J. Jung, T. S. Kim and S. Ryu, *ACS Appl. Mater. Interfaces*, 2022, **14**, 30205–30215.
13 C. J. Chen, Y. X. Zhuang, D. Tu, X. D. Wang, C. F. Pan and R. J. Xie, *Nano Energy*, 2020, **68**, 104329.
14 Y. Jia, M. Yei and W. Jia, *Opt. Mater.*, 2006, **28**, 974–979.
15 N. Terasaki and C. N. Xu, *IEEE Sens. J.*, 2013, **13**, 3999–4004.
16 F. T. Freund, *J. Sci. Explor.*, 2003, **17**, 37–71.
17 Y. Zhou, Y. L. Yang, Y. T. Fan, W. Yang, W. B. Zhang, J. F. Hu, Z. J. Zhang and J. T. Zhao, *J. Mater. Chem. C*, 2019, **7**, 8070–8078.
18 Y. L. Yang, T. Li, F. Guo, J. Y. Yuan, C. H. Zhang, Y. Zhou, Q. L. Li, D. Y. Wan, J. T. Zhao and Z. J. Zhang, *Inorg. Chem.*, 2022, **61**, 4302–4311.
19 Z. J. Zhang, J. T. Zhao, H. H. Chen, Z. Y Man and X. X. Yang, *Chinese Pat.*, 201110155312.6, 2011.
20 Y. Y. Du, Y. Jiang, T. Y. Sun, J. X. Zhao, B. L. Huang, D. F Peng and F. Wang, *Adv. Mater.*, 2019, **31**, 1807062.
21 T. L. Wang, F. Liu, Z. Q. Wang, J. Zhang, S. S. Yu, J. X. Wu, J. H. Huang, W. J. Wang and L. Zhao, *Dalton Trans.*, 2022, **51**, 12290–12298.
22 T. Wang, X. H. Xu, D. C. Zhou, Y. Yang, J. B. Qiu and X. Yu, *Inorg. Chem.*, 2016, **55**, 894–901.
23 A. Bessière, S. Jacquart, K. Priolkar, A. Lecointre, B. Viana and D. Gourier, *Opt. Express*, 2011, **19**, 10131–10137.
24 O. Q. De Clercq, L. I. D. J. Martin, K. Korthout, J. Kusakovski, H. Vrielinck and D. Poelman, *J. Mater. Chem. C*, 2017, **5**, 10861–10868.
25 A. Abdukayum, J. T. Chen, Q. Zhao and X. P. Yan, *J. Am. Chem. Soc.*, 2013, **135**, 14125–14133.
26 F. Liu, Y. F. Chen, Y. J. Liang and Z. W. Pan, *Opt. Lett.*, 2016, **41**, 954–957.
27 H. C. Sun, Q. Zhu and J. G. Li, *Ceram. Int.*, 2022, **48**, 9640–9650.
28 X. H. Zhang, D. Yang, S. F. Wu, X. M. Xu, R. H. Ma, D. F. Peng, Z. L. Wang and S. H. Wang, *Dalton Trans.*, 2022, **51**, 10457–10465.
29 F. Wang and X. G. Liu, *Acc. Chem. Res.*, 2014, **47**, 1378–1385.

30 C. C. Wang, Z. C. Liu, A. N. Yakovlev, T. T. Hu, T. G. Cherkasova, X. D. Zhu, Y. Liu, J. Zhang, D. Y. Liu and X. Yu, *RSC Adv.*, 2023, **13**, 16405–16412.

31 J. Lin, Y. Huang, J. Zhang, F. J. Shi, S. Y. Wei, J. M Gao, Z. X. Huang, X. X. Ding and C. C. Tang, *Mater. Chem. Phys.*, 2008, **108**, 440–444.

32 X. Yu, S. B. Wang, Y. C. Zhu, J. J. Liang, J. B. Qiu, X. H. Xu and W. Lu, *J. Alloys Compd.*, 2017, **701**, 774–779.

33 Y. H. Chen, P. Fan, Z. F. Xu, Q. Luo, Z. J. He, Q. Q. Miao, C. Huang, X. He, Q. Zhang, Z. G. Wang, X. G. Li and L. Li, Anomalous Intense 5d0-7f4 Emission, the Adjustable Emission and Energy Transfer in CaSrGa4O8: Eu3+/Bi3+, *SSRN*, 2022, 4093971.

34 C. C. Zhu, L. Q. Tao, Z. R. Peng, G. Y. Wang, Y. X. Huang, S. M. Zou, H. Sun, Y. F. Zhao, X. P. Chen and T. L. Ren, *Adv. Funct. Mater.*, 2021, **31**, 2103255.

35 S. S. Ding, P. Chen, H. J. Guo, P. Feng, Y. P. Zhou, Y. H. Wang and J. L. Sun, *J. Energy Chem.*, 2022, **69**, 150–160.

36 Y. Xiao, P. X. Xiong, S. Zhang, K. Chen, S. H. Tian, K. Chen, S. H. Tian, Y. S. Sun, P. S. Shao, K. X. Qin, M. G. Brik, S. Ye, D. D. Chen and Z. M. Yan, *Chem. Eng. J.*, 2023, **453**, 139671.

37 B. L. Xiao, P. X. Xiong, S. Wu, D. L. Jiang, K. Chen, Y. Xiao, P. S. Shao and Y. Z. Wang, *Adv. Opt. Mater.*, 2023, **11**, 2300911.

38 T. Hu, Y. Gao, B. Wang, T. Yu, D. W. Wen, Y. Cheng and Q. G. Zeng, *J. Mater. Chem. C*, 2022, **10**, 9554–9562.

39 S. Y. Qin, J. L. Bian, Y. Han, Z. D. Ma, B. Liu, J. C. Zhang, X. H. Xua and Z. F. Wang, *Mater. Res. Bull.*, 2022, **145**, 111535.

40 G. G. Zhang, Y. L. Sun, B. K. Qian, H. Gao and D. Zou, *Polym. Test.*, 2020, **90**, 106670.